BIOMIMETICS

Consecutive aquatic jump-gliding with water-reactive fuel

R. Zufferey[1]*, A. Ortega Ancel[1]*, A. Farinha[1], R. Siddall[1], S. F. Armanini[1], M. Nasr[1], R. V. Brahmal[1], G. Kennedy[1], M. Kovac[1,2†]

Robotic vehicles that are capable of autonomously transitioning between various terrains and fluids have received notable attention in the past decade due to their potential to navigate previously unexplored and/or unpredictable environments. Specifically, aerial-aquatic mobility will enable robots to operate in cluttered aquatic environments and carry out a variety of sensing tasks. One of the principal challenges in the development of such vehicles is that the transition from water to flight is a power-intensive process. At a small scale, this is made more difficult by the limitations of electromechanical actuation and the unfavorable scaling of the physics involved. This paper investigates the use of solid reactants as a combustion gas source for consecutive aquatic jump-gliding sequences. We present an untethered robot that is capable of multiple launches from the water surface and of transitioning from jetting to a glide. The power required for aquatic jump-gliding is obtained by reacting calcium carbide powder with the available environmental water to produce combustible acetylene gas, allowing the robot to rapidly reach flight speed from water. The 160-gram robot could achieve a flight distance of 26 meters using 0.2 gram of calcium carbide. Here, the combustion process, jetting phase, and glide were modeled numerically and compared with experimental results. Combustion pressure and inertial measurements were collected on board during flight, and the vehicle trajectory and speed were analyzed using external tracking data. The proposed propulsion approach offers a promising solution for future high-power density aerial-aquatic propulsion in robotics.

INTRODUCTION

Aerial-aquatic locomotion enables a variety of applications from water sampling during floods to environmental monitoring and disaster response in aquatic environments. Combining multiterrain mobility in a single system enables a variety of consequential applications in oceanography, reservoir management, and agriculture, for which current methods of water monitoring are both time and resource intensive (*1*). This is especially true in remote or dangerous marine environments (e.g., during nuclear accidents, in Arctic regions, or in floodplains) in which aerial-aquatic vehicles can provide samples to a base station over a broad area and can respond more rapidly than single-domain aquatic, aerial, or terrestrial systems. Multimodality (*2*) has been widely demonstrated for aerial-terrestrial (*3*–*8*) and terrestrial-aquatic (*9*–*11*) applications.

Moving in both air and water presents fundamental physical challenges and often conflicting design requirements. The provision of high-power density is a consistent limitation to the application of robots to practical tasks, particularly at the small scale. One of the most power-intensive processes is the transition from water to flight, which requires rapid acceleration to the speed required for flight, due to the presence of additional drag and added water mass.

A principal challenge for aerial-aquatic vehicles is to provide a reliable and robust escape method from water that enables subsequent transition to flight. Recently, several systems have been developed with aerial-aquatic locomotion capabilities but without demonstrating both consecutive and complete transitions to flight from water. In addition, some electric brushless rotor vehicles now have the ability to operate in both media (*12*–*14*), but the transition to flight is typically constrained to very calm sea conditions because they risk being partially or fully submerged by waves that are larger. Implementing aquatic locomotion onto a fixed-wing robot that would transition between air and water dynamically through a high-power thrust bursts offers a low-cost, versatile, and more-efficient solution that could significantly extend the range compared with multirotor vehicles and allow for aquatic escape in a wider variety of conditions.

The transition from water to air is a complex task. Water is three orders of magnitude denser than air, with profound effects on the drag and buoyancy forces in play. Hence, lifting surfaces, such as propellers and wings, cannot operate efficiently in both media, which makes it difficult to accelerate a partially submerged vehicle to flight velocity. Takeoff from water typically requires that the aircraft position its lift and propulsion surfaces well clear of the water to develop aerodynamic forces. A small vehicle, however, is constantly threatened by the possibility of water surface motion, immersing its aerodynamic surfaces with waves that are large relative to its size. A method for producing a high amount of power for a short period of time that is insensitive to water immersion would solve this issue, allowing a vehicle to quickly escape the surface and transition to flight at a safer altitude.

In nature, transition to flight is shown by several animals (*15*, *16*). For example, many fish are also able to shortly leave the surface through accelerating underwater to speeds of 10 m/s and leveraging ground effect for glides above the water surface (*17*). This behavior has, however, not yet been demonstrated by robotic platforms with fin propulsion due to power limitations (*18*). Birds also demonstrate capability of water exit after plunge-diving maneuvers. The gannet, for example, reaches depth because of its momentum and regains altitude with the help of positive buoyancy, energetic flapping, and hydrophobic feathers (*19*). The flying squid achieves full takeoff by rapidly compressing its membrane, producing high-power jetting that is followed by extension of its fins to glide back to the surface (*20*).

[1]Aerial Robotics Lab, Imperial College of London, London, UK. [2]Materials and Technology Centre of Robotics, Swiss Federal Laboratories for Materials Science and Technology, Dübendorf, Switzerland.
*These authors contributed equally to this work.
†Corresponding author. Email: m.kovac@imperial.ac.uk

This jetting occurs by radial contraction of its cavity, driven not only by muscle tissue but also by energy stored in stretched collagen fibers. This allows the squid to produce the high power needed for impulsive aquatic escape, something that has inspired us in the conceptual design (*21*) of this robot.

Impulsive aquatic escape maneuvers necessitate large power reserves for rapid, aggressive acceleration. In robotics, impulsive motion is often addressed with the use of elastic energy storage, compressed gas, or combustible fuels, all of which can rapidly release energy for actuation. Previous studies proposed thrusters using compressed air (*22*) or liquid nitrogen (*23*), but these were also limited to single use and did not include gliding capability. Other relevant research has leveraged and studied jet propulsion for transitionless, underwater locomotion (*24*, *25*).

Combustion offers a means of creating high pressures without the need for a pressurized tank and a release mechanism. Churaman *et al.* (*26*) created robots weighing only 314 mg that were able to jump over 8 cm vertically using explosive actuators. Focusing on aerial-aquatic transitions, researchers have recently shown takeoff of the 100-mg RoboBee by means of hydrogen combustion (*27*). Although those systems showed high-powered thrusts, they required an off-board power supply to function and did not benefit from gliding to prolong the jump. Larger, untethered robots that use combustion to power soft terrestrial jumping robots have been built (*28*–*30*). These systems used pressurized liquid reservoirs of butane gas as fuel, metered into an elastic silicone combustion chamber by electronic valves and ignited by a spark. However, the provision of multiple liquid fuel tanks and flow control apparatus resulted in a significant increase in mass and complexity for a miniature flyable thruster, which would be impractical to integrate into an aerial-aquatic vehicle.

Here, we present a method for producing water jet thrust explosively, as part of an untethered system. It uses a solid fuel reserve to produce combustible acetylene gas that is ignited in a valveless combustion chamber, leading to a powerful, repeatable combustion process that requires only a small pump to move water, sourced from the surrounding environment, through the fuel system. The work presented in this paper makes three contributions to the field of robotics.

First, we present the concept of a novel water thruster for high-power actuation in multiterrain mobility vehicles. It uses the water from the surrounding environment for acceleration by rapidly emptying a partially water-filled combustion chamber. Capable of providing up to 43 N of thrust, it offers a robust way to transition from the surface of the water to flight in a wide variety of conditions through the use of one single actuator. A detailed analysis was performed to obtain optimal performance, giving insight into the diverse physics involved. The proposed system is capable of combining the simplicity of storing fuel in a powder form with the ease of igniting a flammable gas mixture.

Second, we show and validate a flight-capable, lightweight drive system for water jet propulsion. This critical system needs to withstand the high pressures in play and resist the aquatic environment. Multiple challenging tasks are handled simultaneously, including calcium carbide reaction, fuel ignition, high pressure, sensing, and wireless communication. The whole device manages its own power, allowing it to perform untethered operation.

Last, a full demonstration and characterization of the thruster as part of a flying vehicle is presented. The resulting prototype robot performed a total of 22 flights both in a laboratory, under controlled conditions, and outdoors. The four stages of the mission cycle were studied experimentally and are supported by simulations.

RESULTS

Solid reactants as a combustion gas source

Large volumes of fuel gas can be stored compactly as liquid under pressure. However, this requires storage and regulation systems able to sustain large pressures, which adds complexity and makes components heavier. The provision of a pressurized container of combustible gas is also a hazard in and of itself. If the combustible fuel is instead produced by the reaction of two separately stable components, high pressures can be avoided, and the fuel storage and dispensing systems can be greatly simplified. The use of solid compounds for gas storage is common in many applications. One example is the use of sodium azide (NaN_3) decomposition to release nitrogen (N_2) for car airbag deployment. More recently, solid alkali metal hydrides have been explored by the fuel cell industry as a compact means of hydrogen storage.

More relevant to aquatic propulsion are studies undertaken by the U.S. Navy (*31*) examining lithium hydrides for use in a torpedo propulsion system or the work by (*32*) examining solid reactants for buoyancy control. Moreover, the use of water as a reactant is an attractive possibility for aerial-aquatic robots because their environment can be exploited to reduce system mass. Takeoff is not limited to pure water but instead can occur from a variety of water bodies, from stagnant ponds and sediment-filled rivers to salty waters (*33*).

We have developed a fueling and ignition system in which droplets of water are drawn from the surrounding water body and injected into a small container of calcium carbide powder (Fig. 1C). This method permits multiple, separate reactions through the distribution of water droplets. Hence, the total fuel required for the mission can be safely stored in the single container and recharged in a matter of seconds. Counting the water droplets provides a good estimation of the amount of acetylene produced. Acetylene and calcium hydroxide are produced through the following exothermic reaction

$$CaC_2 + H_2O \rightarrow C_2H_2 + Ca(OH)_2$$

The acetylene gas (C_2H_2) is allowed to escape into the partially flooded combustion chamber where it mixes with air. For this process, each milligram of CaC_2 yields 0.3 mg of C_2H_2 for a CaC_2 purity of 75%. Last, the gas mix is ignited by an electric arc, and combustion occurs

$$2C_2H_2 + 5O_2 \rightarrow 4CO_2 + 2H_2O$$

This reaction is highly exothermic, and temperature and pressure increase rapidly in the chamber. This forces the water through a nozzle, out of the combustion chamber, producing the required thrust.

Robot design and mechatronics

The successful implementation of an aerial-aquatic robot that uses combustible gas obtained on board for impulsive takeoff leads to major design challenges. First, the high pressures generated on a small robot impose stress on its structure and hydraulic system. Achieving consistent combustion inside a flooded chamber is not a straightforward process due to the influence of water on ignition and combustion.

Moreover, the robot needs to operate in three distinct modes—jetting, gliding, and water surface operation—which includes landing, data collection, and refilling (Fig. 1A). Each of these stages has significantly different and sometimes conflicting requirements, posing one of the greatest challenges to the design of such robotic

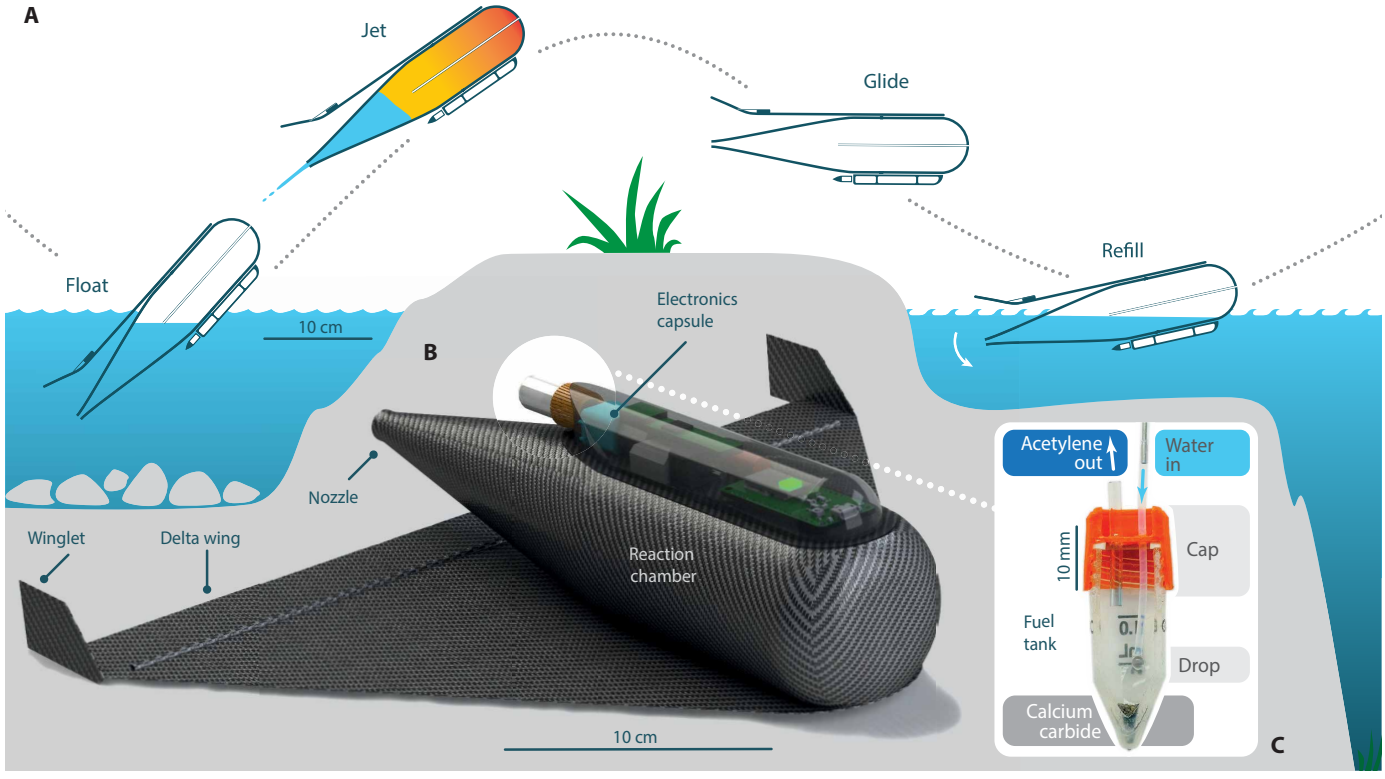

Fig. 1. Mission profile, robot operation, and design. (**A**) Proposed mission stages showcasing the transition from a floating state to an airborne jetting phase and back to floating. (**B**) 3D model render of the underside of the robot highlighting key features. (**C**) Section of fuel container, with fuel for one mission cycle, showing a water drop about to react with the calcium carbide.

platform. This leads to trade-offs at the design stage that limit the performance that can be achieved in each locomotion mode.

For the vehicle to fly in a stable manner during the jetting phase, the center of mass must be a significant distance in front of the center of pressure of the vehicle. However, to maintain a stable floating position on the water surface and the desired angle during jetting, the center of mass must be located behind the center of buoyancy. For the gliding phase, a fine balance between the center of mass and the center of pressure must be struck to achieve static longitudinal flight stability passively. During gliding, the center of mass should be slightly forward from the wing's center of pressure. Further considerations that affect the vehicle configuration are the performance of the propulsion system, the vehicle aerodynamics, and the change in the center of mass during jetting. These distinct conditions and requirements for the different mission phases create design challenges that need to be addressed.

Using the aforementioned principles, our 160-g robot was capable of exiting the water in an uncontrolled environment by reacting 53 mg of calcium carbide with the surrounding water. The reaction generated an average peak pressure of 6.5 bars in 25 ms, which accelerated the robot to 10 m/s, yielding a flight distance of 26 m. The pressure was measured on board during jetting, sharply increasing up to 7.8 bars in 25 ms. The 491-ml composite combustion chamber was filled with 40% of water, which was forced out through a 6.8-mm nozzle. The system emptied in about 200 ms, after which it transitioned to a glide before landing back in the water.

The performance of the propulsion system hinges on various geometric parameters. Total impulse is a key performance metric, which we determined experimentally using submersible load cells. We executed these tests on a static 1:1 model of the robot, further detailed in text S4. This transparent model (Fig. 2A) was also used as a platform for video analysis, because both acetylene production and combustion could be observed inside. The transparent test chamber was designed to have the same geometry as the flying prototype to closely match its jetting characteristics. We measured both the force and the pressure evolution as the robot was attached to a rigid frame. The water-level evolution was simulated numerically (Fig. 2B) and was found to closely agree with the analytically computed water level (Fig. 2C).

Physics of jet-gliding

We developed an analytic physics model to gain insight into the pressure evolution and the flight trajectory and to determine various robot parameters and their impacts on the robot's performance. There are two leading physical aspects to the pressure-propelled vehicle problem. First, an external view of the robot explains the flight trajectory based on the forces on the robot. Second, internal considerations allow us to calculate the pressure evolution and thrust. Both sets of equations have to be solved simultaneously due to the coupling of internal and external physics. This coupling happens due to the effect of the vehicle's acceleration on the water in the chamber, which has an influence on the produced thrust. The equations of motion applied to our system yield the following equation:

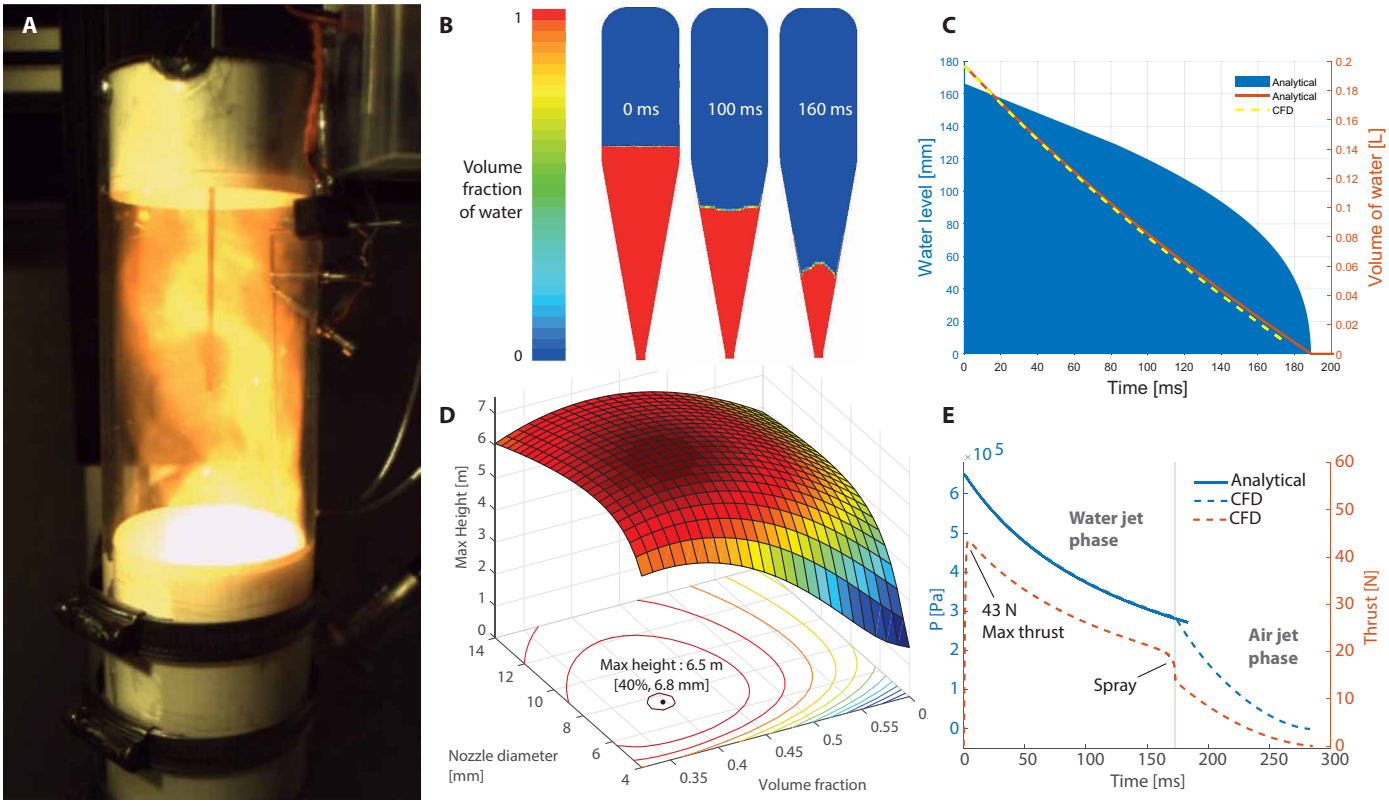

Fig. 2. Jetting phase analysis. (**A**) Combustion during static jetting tests with transparent chamber (movie S5). (**B**) Volume of air (blue) and water (red) in the combustion chamber shown at 0, 100, and 160 ms during the water jetting phase. (**C**) Evolution of the water level and volume during jetting, showing that CFD and analytical predictions compare well. (**D**) Surface plot of analytical model output showing the effect of nozzle diameter and volume fraction on the height achieved by the robot when launched vertically. (**E**) Internal chamber pressure and thrust evolution for the jetting phase.

$$\Sigma\vec{F} = \overrightarrow{\mathrm{Th}} - \vec{W} - \vec{D} - \vec{L}$$

where we consider a two–degree-of-freedom system under the influence of jetting thrust *Th*, tangent to the trajectory, varying weight *W*, as well as drag *D* and lift *L* from the body and the wings. The robot is at this step considered to be a point mass that is traveling in two dimensions (2D). The thrust is given by Euler's flow equation, applied in the chamber from the high-pressure air zone (interface) to the nozzle.

$$\int_{\text{nozzle}}^{\text{interface}} \frac{\partial u}{\partial t}\mathrm{ds} + \frac{\Delta P}{\rho_w} + \frac{1}{2}(u_{\text{nozzle}}^2 - u_{\text{interface}}^2) = 0$$

The pressure ΔP is assumed to follow a dry adiabatic expansion (*34*), and initial pressure P_{init} is given by stoichiometric energy conversion. ρ_w is the water density at 20°C. The flow velocity u is defined at all times and points in the chamber as

$$u(z,r,t) = \frac{\mathrm{dh}}{\mathrm{dt}}\left(\frac{\Omega(h)}{\Omega_{\text{nozzle}}}\right) f\left(\frac{r}{R(z)}\right)$$

The velocity is given as a function of the water level height h, the area of the interface $\Omega(h)$, the distance to the axis r, and the dimension of the chamber $R(z)$. The full derivation of the physics model and its software implementation can be found in texts S1 and S2.

To maximize the jump-gliding performance, we iterated on the analytic model of the full flight presented above, varying the nozzle diameter, volume fraction of water, and launch angle. First, we constrained the system to a 500-ml combustion chamber. This volume corresponds to a stoichiometric mix of acetylene and oxygen using a water drop of 30 mg, or three times the minimum water drop volume that we can produce on board. Although the theoretical ideal combustion pressure of acetylene could reach 13 bars, our static experiments showed a peak gauge pressure of around 7.2 bars. We considered this our reference flight pressure and based our optimization on that value.

The nozzle diameter could be cut to any diameter after fabrication. A larger nozzle results in a higher initial thrust, faster depletion of the chamber, and, consequently, faster mass loss. The initial fraction of water in the chamber has numerous implications. With more water, the weight of the robot is increased but the thrusting phase can last longer. Moreover, the initial water level also changes the floating angle and, consequently, the initial jetting angle.

The most important overall performance metric for the robot is the distance traveled per jetting cycle, which potentially maximizes the usefulness of its mission. The results of the optimization for distance traveled carried out with the physics model are shown in Fig. 2D. The maximum flying distance was achieved with a nozzle of 7.3 mm and a water fraction of 39%. The flight distance did not depend much on nozzle size or volume fraction within a large range of these parameters. A variation of ±1 mm and ±10% water fill changed the total distance by only 3 m, or less than 10%. This gives a wide design space without a major impact on performance. We ultimately cut the nozzle to a diameter of 6.8 mm, yielding a final

total volume of 491 ml, and water fraction of 40%, corresponding to 196.4 ml. Last, the optimal launch angle for maximum flight distance was found analytically to be 47°, and the mass distribution of the robot was altered so that it floated at that set angle.

A 3D computational fluid dynamics (CFD) study of the flow inside the chamber, in the propulsion phase, was carried out to validate the results obtained in the physics model and to understand the flow behavior in 3D. This ensures that the analytic model represents conditions as realistically as possible before manufacturing the robot. The simulation provided insight into the effects of the following physics on performance, which were not included in the 2D analytic model. These included friction of the fluid against the internal walls of the chamber, the thrust produced by the jetting air once the water was evacuated, the irregularity of the water-air interface during jetting, and the effect of water-air spray caused by fluid instabilities at the end of the water jetting phase (*35*). The average reduction in thrust due to shear in the inner walls was shown to be 0.39% in the simulation and hence could be neglected in the model. The 2D analytic model and 3D numerical simulation agree in their prediction of the variation of water volume with time (Fig. 2C) as well as with the evolution of pressure during water jetting (Fig. 2E). The CFD simulations were extended to the air jetting phase. The pressure in the chamber decreased from 6.50 to 2.84 bars during the water jetting phase, whereas the thrust reached a maximum of 43 N and decayed to 20 N after 161 ms, when the jet became a mixture of air and water. As a higher proportion of air started to be ejected, the thrust reduced further to 14 N at 173 ms, when the jet was made up of only air. Because of the lower density of air, pressure and thrust decreased more rapidly during this phase, reaching zero at 285 ms.

Principle of operation

The robot creates acetylene gas from the reaction of calcium carbide with water, after which the ignition is triggered (Fig. 3E). As soon as the robot lands on the water, it starts filling up to the right level due to its low center of mass and venting needle (phase 1). The length of the needle limits how much water can flood the chamber and consequently guarantees that the robot stays afloat at a predefined waterline. Maintaining this preset water line reduces water drag compared with takeoff from a completely submerged state. In addition, wireless communication is guaranteed, something not possible during submersion.

The micro-peristaltic pump is then turned on and produces one droplet every 3.3 s, resulting in a rich gas mix in about 10 s with three drops (phase 2). The droplets react with the fuel quickly, and the resulting acetylene gas escapes into the combustion chamber (phase 3) as the pump blocks the other opening in the reaction chamber. The gas is then ignited with a high-voltage electric arc (phase 4). Thrust is generated as soon as the pressure increases (phase 5).

Figure 3A shows a bottom view of the robot. The driving components fit under a sealed transparent dome, affixed to the composite combustion chamber. The multilaunch fuel container, which can hold fuel for 10 launches, rests at the interface to permit reloading without the need to open the dome. A high delta wing, elevator, and vertical wingtip fins were attached on the opposite side of the chamber.

The combustion chamber was designed with a rounded top followed by a straight cylindrical section, a 20° conical section ending on a nozzle (Fig. 3D). The chamber was designed to withstand 8 bars of internal pressure, following the results from the static experiments.

The electronics were encapsulated in a waterproof module. Inside, a microcontroller was connected to its actuators (Fig. 3C). The water droplets were created by a peristaltic pump, which drew water from the surrounding environment. This pump has proven to be extremely reliable in real-world conditions. A gauge pressure sensor measured the chamber pressure after ignition. Last, we required an ignition source. The consistent ignition of the acetylene is a challenge at small scales, especially at ambient pressure and with a half-flooded chamber. Hydrogen ignition at smaller scales has been demonstrated (*27*) with the help of an off-board power supply. Previous research generated a spark from a piezoelectric element compressed by a shape-memory alloy wire (*36*). This mechanically actuated system wore out quickly due to the high forces in play. Our robot solves the ignition issue with solid-state electronics that consist of a feedback transformer and a power transistor to create a pulsed electric arc of 3 mm. Several ignition methods were researched (text S3). The whole system is powered by a 270-mAh lithium battery.

The robot was controlled by Adafruit's Feather board (Fig. 3B). This microcontroller board combines an ARM M0 processor with a Bluetooth low-energy chip. At 5.8 g, this board is a good trade-off between low weight, sufficient number of inputs, and wireless communication. Most onboard functions were executed at predetermined times. Simultaneously, the robot captured inertial and pressure data (fig. S1). The inertial measurement (IMU) sensor fusion was realized on chip, and the resulting data were recorded at 100 Hz. The gauge pressure sensor was read at a 2-kHz rate and provided accurate values despite the harsh conditions.

The wing was made of a 0.2-mm-thick flat carbon fiber plate with fibers in a 2/2 twill weave, oriented span wise and chord wise. A high wing configuration was used to ensure roll stability, and two vertical stabilizers were located on the wingtips to reduce induced drag. Pitch stability was ensured by performing a CFD analysis and studying the static stability of the robot in flight (fig. S3). The delta wing configuration resulted in two vortices forming along the leading edges at high angles of attack, which then traveled over the wing (Fig. 3B). This feature is a major advantage when compared with a regular rectangular wing, delaying flow separation at high angles of attack and creating large suction at the top surface, enabling higher lift coefficients as a consequence. The robot was able to generate enough lift for relatively small wingspans, keeping the weight of the system to a minimum.

Performance and flight operation

Controlled flight experiments were performed in an indoor flight laboratory equipped with 16 Vicon tracking cameras, with which position was measured (fig. S2). The robot launched from a water tank into a net for impact protection. The jetting phase, as well as the initial part of the trajectory, was accurately studied. The gray circles visible on the fins were 2D reflective markers for the tracking system. We used 10 reflective markers to take these measurements, which can be seen in Fig. 4 (A and E).

We show that the robot would upright itself to the designed angle of 47° when it landed in the water due to its center of gravity being behind the center of buoyancy. As soon as it rested on the water surface, the nozzle was underwater and the chamber started to fill up. The time spent refilling could be spent on the robot's main mission, e.g., taking water measurements or sampling data. Once the orientation of the robot matched the expected angle, the launch sequence was triggered, and the robot took off.

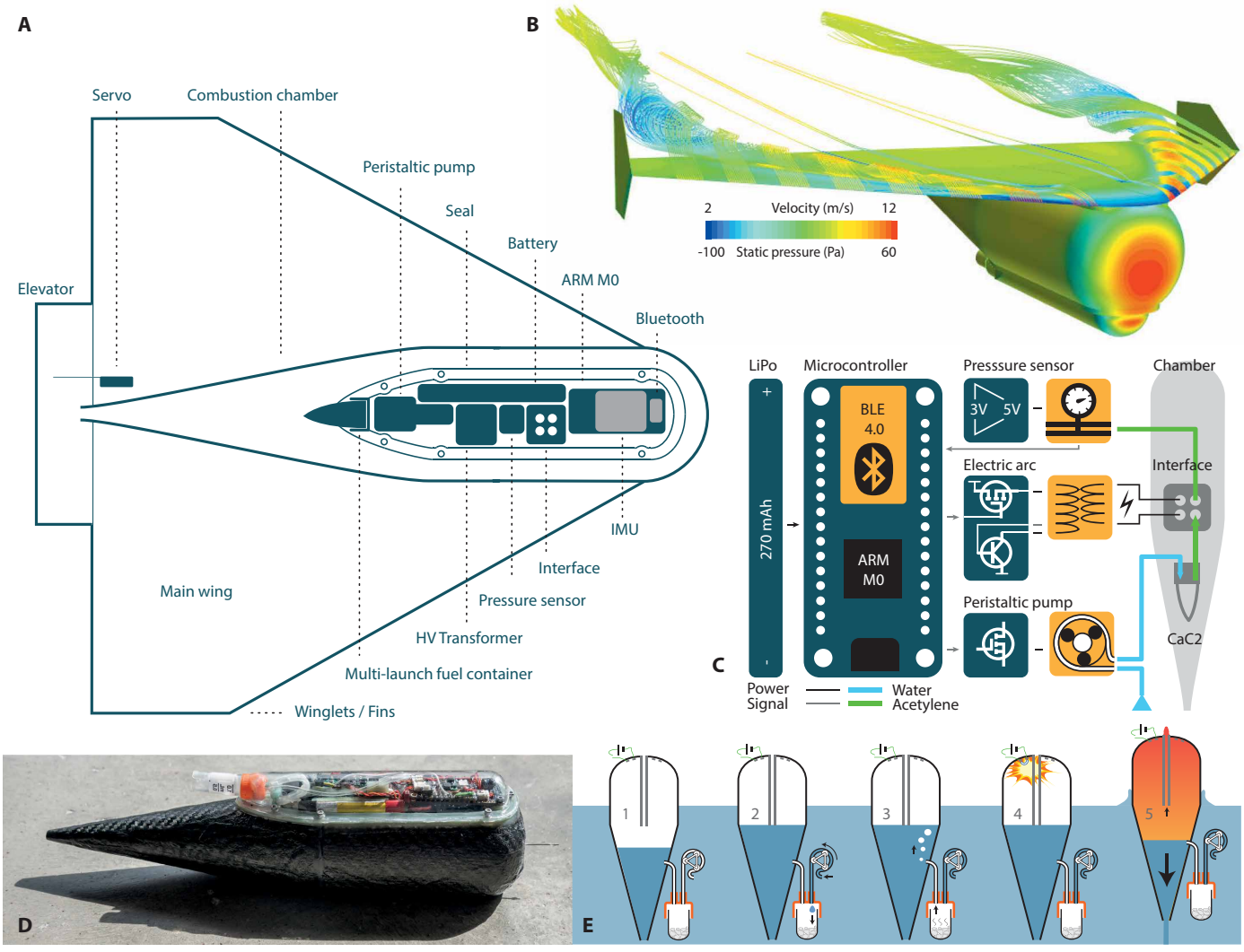

Fig. 3. Overview of the aerial-aquatic robot systems. (**A**) Bottom view schematics of the aircraft with the electronics on top of the combustion chamber. (**B**) Static pressure contours on robot body, and streamlines colored by velocity magnitude for a simulation at 8° angle of attack and freestream velocity of 10 m/s. (**C**) System diagram of the onboard electronics and transducers. (**D**) Side view photograph of the assembled jetting system showing the electronics under their transparent waterproof cover. (**E**) 1, water intake; 2, water pumping into fuel tank; 3, reaction to produce acetylene gas; 4, ignition; 5, water jetting, showing choked needle.

We compared the velocity of the robot during the initial stages of flight between the analytical model output and the tracking system measurements (Fig. 4B). The tracked velocity can be seen to follow the modeled velocity closely, being slightly slower at the end of jetting and beginning of gliding. This is linked to chamber deformation under high pressures, wing bending (which has a major impact on flight angle), pressure losses, and variability in precombustion gas mixing. The displayed velocity was obtained from the tracked trajectory, which is available in fig. S8. The robot's trajectory was shorter than modeled due to the slightly lower velocity achieved at the end of the jet.

The corresponding accelerations are also displayed in Fig. 4B (tracked and predicted) and agree well, albeit with a sharper drop at the end of the jet in the model, which did not consider air thrust. IMU from three separate flights shows acceleration profiles in agreement with tracking data, with some variability stemming from launch angle inaccuracy and jetting differences between experiments. The onboard sensor saturates at 4 g, as indicated by the dotted black line and samples at 100 Hz.

We note that, in the model, the jetting stopped earlier and more abruptly than in the experiments, at about 200 ms, because it did not take into account the spraying or air jetting as described in the "Physics of jet-gliding" section. The measured duration of jetting ended at 285 ms, which is consistent with the CFD simulations. Tracking stopped just after 600 ms, when the robot left the field of view of the cameras.

Flight testing

Outdoor water exit was recorded from a pond that has a depth of 1 m at the launch position and is subject to outdoor, gusty conditions. The robot was oriented in a specific direction for video capture and was loosely kept in place by two rods to avoid drifting. The control commands were sent from shore. We show the robot in flight during four key phases of the water takeoff (Fig. 5A). In the first stage, it

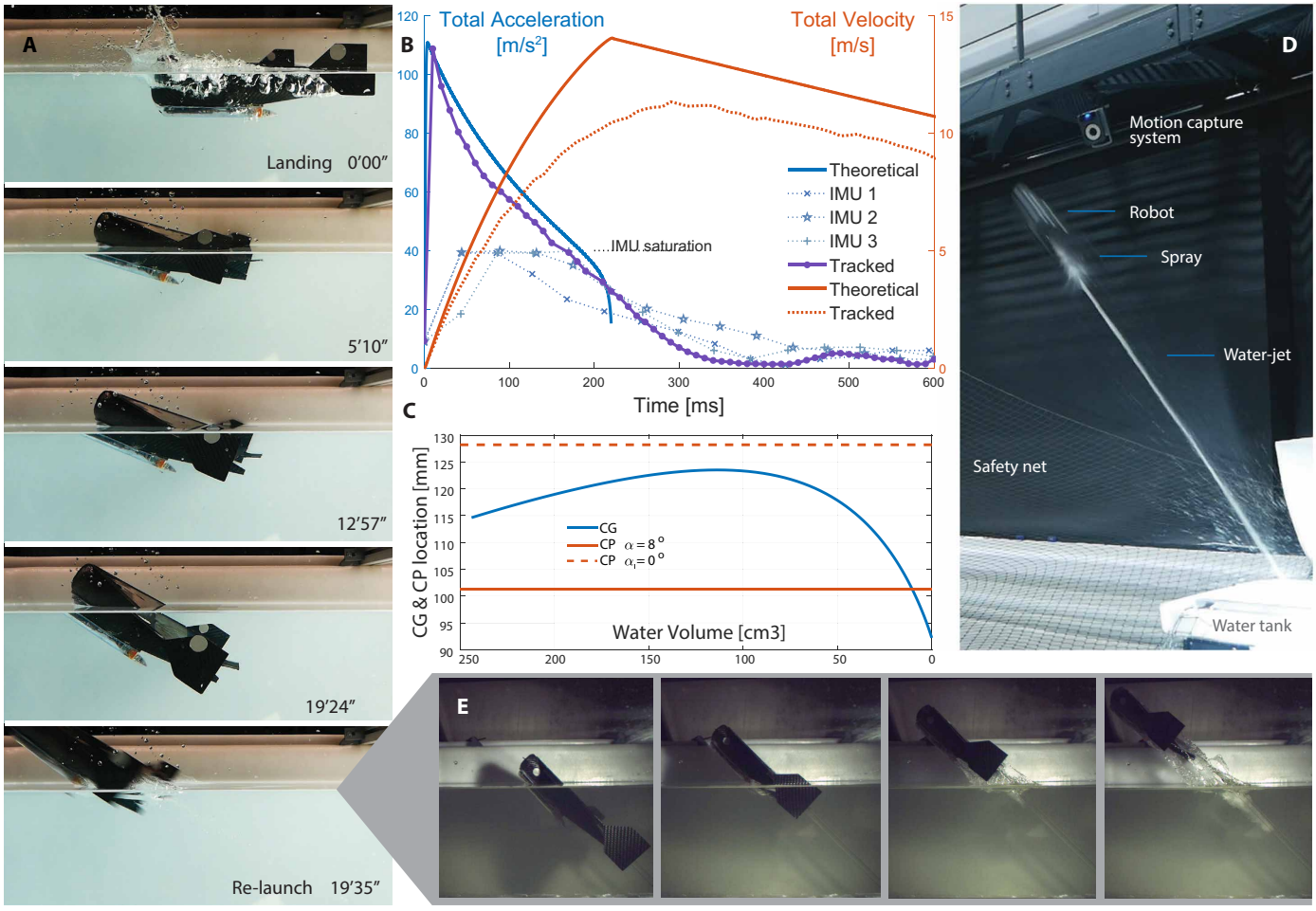

Fig. 4. Laboratory tests. (**A**) Time lapse of the landing process, refilling process, and subsequent launch. (**B**) Comparison of position and velocity profiles for the experiment and the analytical model. (**C**) Evolution of the position of the center of gravity as the robot empties, moving ahead of the center of lift. (**D**) Capture of a high-powered launch in the flight arena at the end of the water jetting phase (movie S2). (**E**) Robot during water escape (movie S3).

fills up with water while venting air through the top needle. As the pressure in the chamber increases, thrust is generated and the robot exits the water. The jetting continues in air during the first 200 ms of flight. Once the chamber is empty, spray is visible for a short period until the pressure equalizes, as shown in the last time shot.

We report three different pressure measurements taken during flight by the onboard pressure sensor (Fig. 5B). The onboard recorded pressure was validated with the off-board sensor (Honeywell 40PC series) installed during static tests, read by means of an acquisition board and LabVIEW. The pressure peaks achieved varied between tests by a maximum of ±15% of the peak pressure, consistent with different fuel mixes. The exact gas mix ratio depended on the dispersion of water droplets onto the calcium carbide, which varied with the tube surface tension, orientation of the robot, and vibrations. In addition, visual recording of the combustion process showed significant differences in the evolution of the flame front (Fig. 2A), which had an impact on the recorded pressure peak. Last, the peak might reach higher values between measurements as the sensor operates at 2 kHz. We also observed that, although successful takeoff was possible with changing wind speed and direction, wind gusts created variance in the overall flight distance. The wind was recorded to be an average of 5 m/s with gusts of 7.5 m/s.

We present a flight trajectory in which the robot exits the water level to land on grass (Fig. 5C). The robots performed seven consecutive flights in this set of testing. Because of the small size of the pond, the robot was manually taken from the grass and placed back in the pond for each flight.

DISCUSSION

This research presents a new combustion-driven water jet thruster for jump-gliding locomotion. We also show a detailed analysis of the underlying physics and the influence of the main design parameters on performance, as well as validation against CFD results and static combustion experiments. The study was completed by the development of an untethered jump-gliding robot, and we include a description of the mechanical systems, software, and electronics. We demonstrate its capability to consecutively launch from water. The robot was shown to operate in both laboratory and outdoor conditions over 22 flights, achieving a maximum flight distance of 26 m, rising to a maximum height of 8.3 m, and reaching maximum thrust,

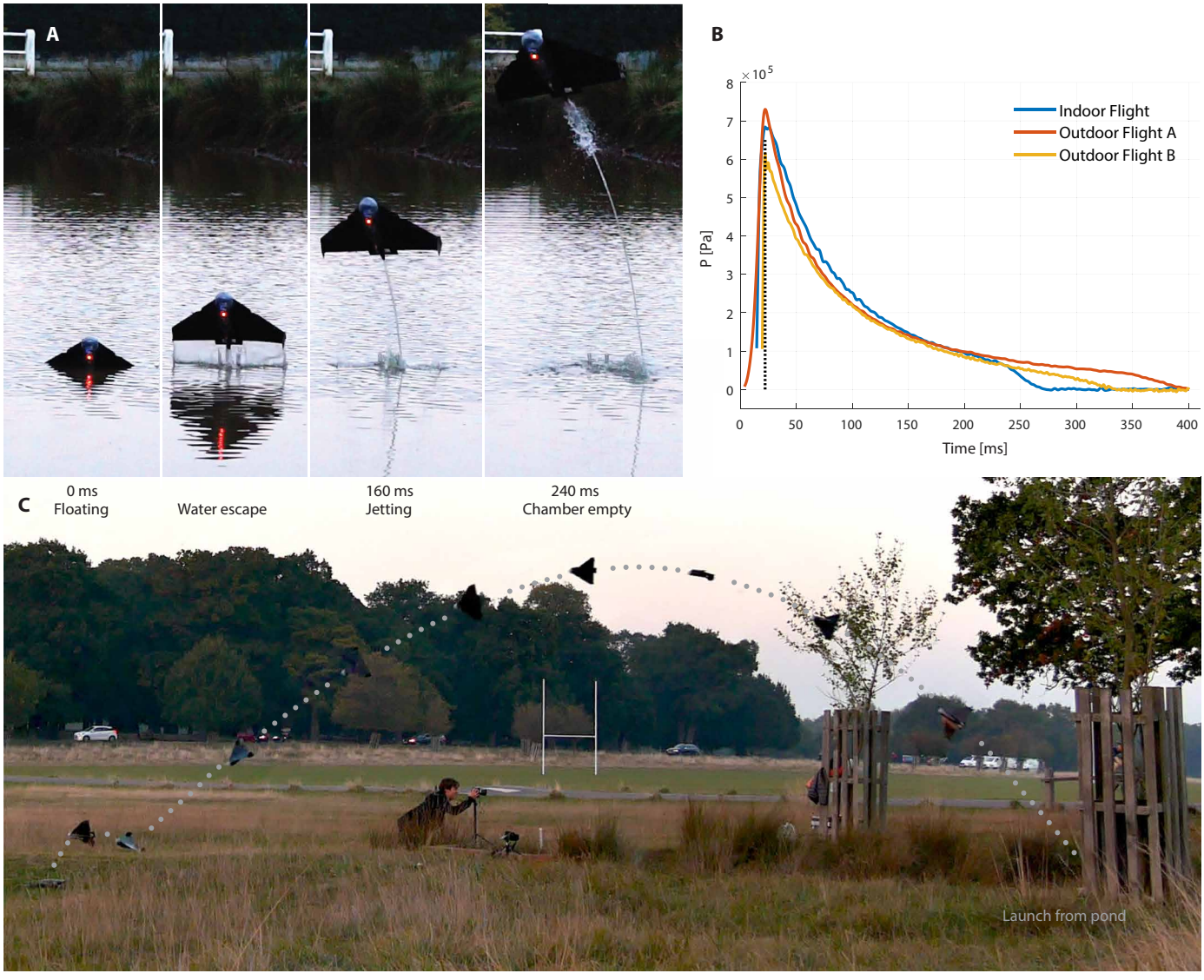

Fig. 5. Outdoor flight tests. (**A**) Composite image of the robot in floating, jetting, and flying mode (movie S4). A bystander on the sidewalk was edited out for clarity. (**B**) Pressure evolution of indoor and outdoor flights aligned at pressure peak. (**C**). Flight trajectory of a pond-to-grass launch.

peak pressure, acceleration, and velocity of 7.8 bars, 50.2 N, 110 m s^{-2}, and 11 m s^{-1}, respectively. Such performance is possible due to the robot's unique propulsion system and reliance on a single actuator, which triggers the reaction and combustion process. This also makes the entire system simple to waterproof, increasing its reliability.

High-powered aquatic escape is a phenomenon also observed in nature, which occurs through a large range of animal length scales. Jumping height approximately correlates with size as height/length $\propto$ length$^{-1/3}$. This is shown in (*15*) for a wide range of impulsive, mixed, and momentum-driven water-jumping animals, bioinspired robots, and blunt bodies. We show in fig. S9 the estimated jumping height of the robot at 90° compared with impulsive jumping animals in (*15*), squid flight in (*22*), and water-jumping robots (*15*, *16*, *27*, *35*, *37*). Although jetting robots perform two to five times better than their biological counterparts, legged robots perform poorly relative to nature. This is likely a result of the high-power densities of jetting robots and their ability to produce thrust in air, where drag is reduced. The comparison hints that, although flying squids and jetting robots operate very differently from their legged counterparts, they broadly follow the same $L^{-1/3}$ trend. However, we note that data on both flying squid and jetting robots are currently scarce and that sound conclusions on the scaling of full systems will become possible as the field matures.

The analysis and findings in this paper can be used in the development of future aerial-aquatic robots. With the addition of the necessary control systems, autonomous flying can already be achieved. For range extension, a low-power propeller would allow the robot to cross larger areas of water or even reach other lakes. The integration of a switchable gearbox (*38*) to the propeller could permit efficient locomotion both in water and in air. With the addition of enhanced actuation and control, the applicability of the robot would be significantly increased, cruising autonomously from one sampling point to another.

A limitation of the current robot is the filling time required between repeated launches, which is an average of 20 min, whereas the volume of air vents through a 505–μm–inner diameter needle. This time could be shortened by increasing the diameter of the venting needle. However, this would increase the losses during jetting, something we prioritized over shorter filling times. The installation of a passive one-way venting valve would reduce the larger losses resulting from a larger diameter needle at the expense of additional weight, complexity, and the reliability inherent to the valveless combustion chamber design. This trade-off was not considered worthwhile for this study but would be significantly more important for a prototype optimized for field operation. Last, the robot currently has no means of detecting that the chamber is filled to the expected level before launch. This step may become unsupervised with further sensor integration.

The thruster presented in this research has been demonstrated to perform multiple aquatic takeoffs, from a tank and from an outdoor pond. Because of its impulsive actuation force of more than 25 times the robot's weight, it is relatively insensitive to the water surface state and can jet off in wavy conditions. We report that the robot will successfully escape the water when angled between 10° and 90°, based on modeling and confirmed by experiments. The robot's rotation has been tracked experimentally for various wave sizes and periods (fig. S7). We note that if the robot is hit by a particularly steep wave from the front, which is the most critical case, it will tip over and takeoff becomes impossible. This occurs for waves with a large height to period ratio, as shown in fig. S5. Nonetheless, the robot exhibits a good expected flight performance at most points in different waves, as reported in fig. S9.

MATERIALS AND METHODS

Combustion chamber fabrication

Because the combustion chamber is a thin-walled pressure vessel, the hoop stress in the wall can be approximated by the Young-Laplace equation:

$$\sigma \approx \frac{Pr}{t}$$

where σ is the hoop stress, P is the internal chamber pressure, r is the chamber radius, and t is the wall thickness. Using this equation, with a maximum chamber pressure of 750 kPa and a tensile strength of the carbon fiber composite of 645 MPa, the required thickness was calculated to be 35 μm. Therefore, we decided to use two layers of XC130 210 gsm pre-preg woven carbon fiber composite, yielding a minimum thickness of 200 μm. This allows a considerable margin for manufacturing defects, as well as stress concentrations from the chamber design, which includes two flat sections to hold the electronics capsule, visible in the top part of Fig. 1B, and the wing.

The combustion chamber is a hollow shape, combining a nozzle, conical section, quasi-cylindrical section, and a dome. The chamber shell was built in two parts, overlapping in the straight section. The manufacturing of such a body was done in three parts. We manufactured two separate inside molds from aluminum, with a slightly wider top mold. Using inside molds gives a smooth inside surface of the chamber, which reduces flow losses. In addition, the molds have two 40-mm-wide flats on each side, one where the electronics module is bonded and one for the wing attachment.

Carbon fiber preimpregnated with resin was wrapped around the two molds. Special care was taken that the necessary cuts in the fiber did not overlap. Once the two shells were cured and removed from the mold, the interface inserts were installed in the top shell and the overlap section was sanded. Last, the shells were bonded together, the needle was installed, and the nozzle was accurately machined to specification.

Electronics driver module fabrication

A 3D-printed nylon frame was permanently bonded with flexible epoxy to the combustion chamber. This part not only held every individual component but its edge was also the support for the seal. Last, there were six screw inserts in the frame to attach the top dome. This dome was a vacuum-formed high-impact polystyrene 0.75-mm transparent shell that was screwed to the frame, compressing a custom 1-mm silicone seal. The whole assembly is fully submersible and visible due to its transparency. The calcium carbide tank consisted of a 1-ml chemical test tube, with one Teflon tube for water inlet and one polyvinyl chloride tube for gas outlet, both through the cap of said tank. This cap was epoxied to the dome.

A removable plate interfaced the electronics module with the combustion chamber. This device increased the lifetime of the robot significantly, making repairs and inspections straightforward. The sealed carbon fiber plate was water jet cut and bolted to preinstalled screws welded to the inside of the chamber. It bore the acetylene gas inlet, the pressure tube connection, and two insulated high-voltage electrodes. The micro-peristaltic pump's DC motor (RP-Q1 Takasago Fluidic Systems) ran on regulated 3.3 V for constant speed. It was driven by the microcontroller via a 1-A MOSFET. Smaller droplets provided a better count of the amount of water dispersed per second. For that reason, a Teflon tube was attached to the outlet, creating 8-ml droplets every 3 s.

The plasma driver was turned on via a separate MOSFET. Once the device is connected to the battery voltage, a power transistor shorts the primary coil of the transformer. The magnetic field increases in the transformer until the power transistor cuts off the primary via the feedback coil. The magnetic energy is released as current, i.e., secondary, generating a high-voltage spike. As soon as the induced feedback voltage drops, the power transistor shorts the primary and the cycle starts again. Although the driver operated as expected in dry air conditions, it had some shortcomings when located in the robot. The electrode tips were eroded by the electric arc, and the short distance between them made it vulnerable to a water drop staying attached. Those issues were mitigated by reducing the arc duration to 300 ms and moving the electrode closer to the top of the chamber. Last, because the arc was pulsed at around 15 kHz, radio frequency interference with the wireless operation of the robot was problematic. Without proper shielding, the Bluetooth chip reset when the arc was enabled. Brass shielding and coaxial electrodes are essential to prevent this interference. Other ignition mechanisms have been explored and tested (see text S3).

The robot has an onboard 2.4-GHz communication link running the Bluetooth 4.0 protocol. The electronic capsule was arranged so that the antenna faced the top of the robot or else the signal was weakened by absorption in the water. The Bluetooth link was set up as a UART tunnel, transmitting serial data directly to a central mode device—in our case, a phone. The control of the launch happened in three distinct phases. First, default flight parameters could be changed before launch, e.g., water amount reacted. Second, launch was initiated. After the experiment was over, recorded data were streamed back to the connected device.

Wing design and stability

The multimodal capabilities of the platform introduced conflicting requirements for its design, which were linked to the different dynamics that describe its locomotion stages. The wing's geometry was used as the last design variable to ensure good behavior of the platform throughout its operation.

A reasonable solution to the conflicting trade-offs that control this design was the use of adaptive morphology by changing the robot's shape to ensure the best performance in different operating conditions. Although this design principle may potentially improve overall performance, it would be done at the expense of additional weight and complexity. It was decided, instead, to balance these wing design trade-offs through an analysis of its effect on the different mission phases.

The buoyancy was studied using the mass properties from a 3D model of the robot. The dynamics of the system were simplified, taking only the weight and the buoyancy force in the vertical plane. The buoyancy force was estimated by taking the fixed breathing needle length and iterating immersion depths and flotation angles in the model. This permitted the calculation of the total water volume displaced and, consequently, the buoyancy force and center of buoyancy. These were evaluated to identify the static stable equilibrium configuration of the system. This equilibrium configuration corresponded to the values of immersion depth and angle for which the value of the buoyancy force equaled the weight, and the center of buoyancy of the robot produced no moment around the center of mass. Moreover, the stability condition during floating was that the center of buoyancy was located above the center of mass. Further details can be found in text S5.

The wing was thus designed as a denser-than-water, yet light, thin plate with the center of mass located toward the back of the robot. An uncambered thin plate was used because it generated no lift at a 0° angle of attack and lower drag during jetting at the air-water interface. Half circle unidirectional carbon fiber rods were used as stiffeners to ensure stability in flight.

A delta wing geometry was used because it delayed stall when compared with a regular rectangular wing and because its center of pressure varied with the angle of attack, positively affecting the robot's stability during both flight stages. This property allowed the robot to keep its center of pressure behind the center of mass for any volume of water inside the chamber while also maintaining a static margin during gliding that allows reasonable maneuverability. An elevon, which counteracts the moment generated by the lift and drag, was added to the back of the wing. Its angle was set to a fixed value so that gliding occurred at 8°, the sustained gliding angle at 10 m/s.

Numerical simulations were performed to calculate the wing area necessary to achieve sustained gliding and to ensure pitch stability of the robot during gliding and jetting. The static stability of the robot in flight was ensured by obtaining negative derivative of the pitching moment with the angle of attack, and the calculated sustained gliding angle was obtained as 8° for a velocity of 10 m/s, which corresponds to the maximum glide ratio of the robot (fig. S3).

Numerical simulation setup

The simulation setup, calculation of the solution, and postprocessing for both internal and external flow simulations were carried out with STAR-CCM+ 12.06.010-R8. For the jetting flow simulations, we used a slightly simplified model of the combustion chamber, with a circular chamber cross-section and without the venting needle. We restricted the domain to the inside of the combustion chamber only and set the boundary conditions as no-slip walls for the chamber walls and pressure outlet at atmospheric pressure for the nozzle outlet. We defined the initial conditions as the top 60% of the chamber volume being air at 6.5 kPa gauge pressure, taken as a representative value from the static testing, and the bottom 40% as water at atmospheric pressure. We assumed no heat transfer.

We generated the mesh using the polyhedral mesher and surface remesher with a base size of 4 mm. To resolve the air-water interface adequately, we used a volumetric refinement, of a relative cell size of 50% of the base, for the nozzle and a further refinement, of a relative cell size of 20% of the base, around the initial position of the air-water interface. We also added a prism layer of 1.6-mm thickness consisting of three layers along the chamber walls. We used the volume of fluid (VOF) multiphase model with VOF-VOF interaction. The maximum Reynolds number based on the nozzle diameter for the water flow is 248,500. However, the flow was in a strong forward pressure gradient; therefore, the flow was expected to be laminar and was treated as such in the simulation.

In the external aerodynamics study, a segregated (SIMPLE-type) solver was used to solve the incompressible Reynolds-averaged momentum conservation equations. Menter's two equation model standard k-ω SST (shear stress transport) was used for the modeling of turbulence. The thermophysical properties of air used for the calculations were taken for 20°C at 1 atm. Domain and mesh convergence studies were performed using different domain lengths and widths, as well as varying meshes. An hexahedra mesh with a base size of 5 mm with a dense wake refinement region was used, and 3 to 12 laminar layers were used to capture the boundary layer. The used boundary conditions are the following: constant velocity zero gradient pressure inlet, constant pressure zero gradient velocity outlet, constant pressure, calculated velocity side walls with reflux velocity extrapolated from domain, and no slip on the robot model. A hybrid wall function was used, with a wall function being active for the regions where the first cell lay within the buffer or logarithmic layer.

SUPPLEMENTARY MATERIALS

robotics.sciencemag.org/cgi/content/full/4/34/eaax7330/DC1

Text S1. Analytic model derivation
Text S2. Physics model implementation
Text S3. Ignition study
Text S4. Transparent static model development
Text S5. Floating stability
Fig. S1. Embedded code structure.
Fig. S2. Laboratory setup.
Fig. S3. Flight performance.
Fig. S4. Buoyancy stability.
Fig. S5. Possible launch range in waves.
Fig. S6. Robot behavior in waves.
Fig. S7. Inclination and expected performance in waves.
Fig. S8. Tracked laboratory fight trajectory.
Fig. S9. Animal and robot water-jumping height comparison.
Table S1. Animal and robot water-jumping height comparison.
Movie S1. Assembly.
Movie S2. Laboratory flight tests at different angles.
Movie S3. Demonstration of impulsive water escape.
Movie S4. Demonstration of outdoor flights.
Movie S5. Acetylene combustion tests.
Movie S6. Demonstration of indoor flight with a launcher.
Movie S7. Demonstration of landing and relaunching.
Movie S8. Wave tests.

REFERENCE AND NOTES

1. D. Floreano, R. J. Wood, Science, technology and the future of small autonomous drones. *Nature* **521**, 460–466 (2015).
2. K. H. Low, T. Hu, S. Mohammed, J. Tangorra, M. Kovač, Perspectives on biologically inspired hybrid and multi-modal locomotion. *Bioinspir. Biomim.* **10**, 020301 (2015).
3. Z. Zhakypov, K. Mori, K. Hosoda, J. Paik, Designing minimal and scalable insect-inspired multi-locomotion millirobots. *Nature* **571**, 381–386 (2019).
4. A. L. Desbiens, M. T. Pope, D. L. Christensen, E. W. Hawkes, M. R. Cutkosky, Design principles for efficient, repeated jumpgliding. *Bioinspir. Biomim.* **9**, 025009 (2014).
5. L. Daler, J. Lecoeur, P. B. Hählen, D. Floreano, A flying robot with adaptive morphology for multi-modal locomotion, in *2013 IEEE/RSJ International Conference on Intelligent Robots and Systems* (IEEE, 2013), pp. 1361–1366.
6. M. A. Woodward, M. Sitti, MultiMo-Bat: A biologically inspired integrated jumping-gliding robot. *Int. J. Robot. Res.* **33**, 1511–1529 (2014).
7. A. Vidyasagar, J.-C. Zufferey, D. Floreano, M. Kovač, Performance analysis of jump-gliding locomotion for miniature robotics. *Bioinspir. Biomim.* **10**, 025006 (2015).
8. K. Peterson, P. Birkmeyer, R. Dudley, R. S. Fearing, A wing-assisted running robot and implications for avian flight evolution. *Bioinspir. Biomim.* **6**, 46008 (2011).
9. Y. Chen, N. Doshi, B. Goldberg, H. Wang, R. J. Wood, Controllable water surface to underwater transition through electrowetting in a hybrid terrestrial-aquatic microrobot. *Nat. Commun.* **9**, 2495 (2018).
10. A. Crespi, A. Badertscher, A. Guignard, A. J. Ijspeert, AmphiBot I: An amphibious snake-like robot. *Robot. Autonom. Syst.* **50**, 163–175 (2005).
11. W. Hu, G. Z. Lum, M. Mastrangeli, M. Sitti, Small-scale soft-bodied robot with multimodal locomotion. *Nature* **554**, 81–85 (2018).
12. H. Alzu'bi, I. Mansour, O. Rawashdeh, Loon Copter: Implementation of a hybrid unmanned aquatic-aerial quadcopter with active buoyancy control. *J. Field Robot.* **35**, 764–778 (2018).
13. M. M. Maia, P. Soni, F. J. Diez, Demonstration of an aerial and submersible vehicle capable of flight and underwater navigation with seamless air-water transition. arXiv:1507.01932 (2015).
14. R.-A. Peloquin, D. Thibault, A. L. Desbiens, Design of a passive vertical takeoff and landing aquatic UAV. *IEEE Robot. Autom. Lett.* **2**, 381–388 (2017).
15. B. Chang, J. Myeong, E. Virot, C. Clanet, H.-Y. Kim, S. Jung, Jumping dynamics of aquatic animals. *J. R. Soc. Interface* **16**, 20190014 (2019).
16. J.-S. Koh, E. Yang, G.-P. Jung, S.-P. Jung, J. H. Son, S.-I. Lee, P. G. Jablonski, R. J. Wood, H.-Y. Kim, K.-J. Cho, Jumping on water: Surface tension–dominated jumping of water striders and robotic insects. *Science* **349**, 517–521 (2015).
17. J. Davenport, How and why do flying fish fly? *Rev. Fish Biol. Fish.* **4**, 184–214 (1994).
18. L. Wen, T. Wang, G. Wu, J. Liang, Quantitative thrust efficiency of a self-propulsive robotic fish: Experimental method and hydrodynamic investigation. *IEEE/ASME Trans. Mechatron.* **18**, 1027–1038 (2013).
19. S. Garthe, S. Benvenuti, W. A. Montevecchi, Pursuit plunging by northern gannets (Sula bassana) feeding on capelin (Mallotus villosus). *Proc. R. Soc. Lond. Ser. B Biol. Sci.* **267**, 1717–1722 (2000).
20. R. O'Dor, J. Stewart, W. Gilly, J. Payne, T. C. Borges, T. Thys, Squid rocket science: How squid launch into air. *Deep Sea Res. II Top. Stud. Oceanogr.* **95**, 113–118 (2013).
21. M. Kovac, The bioinspiration design paradigm: A perspective for soft robotics. *Soft Robot.* **1**, 28–37 (2014).
22. R. Siddall, M. Kovač, Launching the AquaMAV: Bioinspired design for aerial-aquatic robotic platforms. *Bioinspir. Biomim.* **9**, 031001 (2014).
23. J. Mo, Z. Miao, B. Li, Y. Zhang, Z. Song, Design, analysis, and performance verification of a water jet thruster for amphibious jumping robot. *Proc. Inst. Mech. Eng. C J. Mech. Eng. Sci.* **233**, 5431–5447 (2019).
24. L. Jian, Z. Jianing, W. Zhenlong, CFD simulation of effect of vortex ring for squid jet propulsion and experiments on a bionic jet propulsor. *IJUNESST* **9**, 211–226 (2016).
25. F. G. Serchi, A. Arienti, I. Baldoli, C. Laschi, An elastic pulsed-jet thruster for soft unmanned underwater vehicles, in *2013 IEEE International Conference on Robotics and Automation* (IEEE, 2013), pp. 5103–5110.
26. W. A. Churaman, L. J. Currano, C. J. Morris, J. E. Rajkowski, S. Bergbreiter, The first launch of an autonomous thrust-driven microrobot using nanoporous energetic silicon. *J. Microelectromech. Syst.* **21**, 198–205 (2012).
27. Y. Chen, H. Wang, E. F. Helbling, N. T. Jafferis, R. Zufferey, A. Ong, K. Ma, N. Gravish, P. Chirarattananon, M. Kovac, R. J. Wood, A biologically inspired, flapping-wing, hybrid aerial-aquatic microrobot. *Sci. Robot.* **2**, eaao5619 (2017).
28. M. T. Tolley, R. F. Shepherd, M. Karpelson, N. W. Bartlett, K. C. Galloway, M. Wehner, R. Nunes, G. M. Whitesides, R. J. Wood, An untethered jumping soft robot, in *IEEE International Conference on Intelligent Robots and Systems* (IEEE, 2014), pp. 561–566.
29. N. W. Bartlett, M. T. Tolley, J. T. B. Overvelde, J. C. Weaver, B. Mosadegh, K. Bertoldi, G. M. Whitesides, R. J. Wood, A 3D-printed, functionally graded soft robot powered by combustion. *Science* **349**, 161–165 (2015).
30. M. Loepfe, C. M. Schumacher, U. B. Lustenberger, W. J. Stark, An untethered, jumping roly-poly soft robot driven by combustion. *Soft Robot.* **2**, 33–41 (2015).
31. H. L. Newhouse, P. R. Payne, *Underwater Power Source Study* (Payne Inc., 1981).
32. J. Borchsenius, S. Pinder, Underwater glider propulsion using chemical hydrides, in *OCEANS 2010 IEEE Sydney*, Sydney, NSW, Australia, 24 to 27 May 2010.
33. R. E. Threlfall, *The Story of 100 Years of Phosphorus Making 1851–1951* (Albright & Wilson, 1951).
34. C. J. Gommes, A more thorough analysis of water rockets: Moist adiabats, transient flows, and inertial forces in a soda bottle. *Am. J. Phys.* **78**, 236–243 (2010).
35. R. Siddall, M. Kovac, Fast aquatic escape with a jet thruster. *IEEE/ASME Trans. Mechatron.* **22**, 217–226 (2017).
36. R. Siddall, G. Kennedy, M. Kovac, High-power propulsion strategies for aquatic take-off in robotics, in *Robotics Research*, A. Bicchi, W. Burgard, Eds. (Springer Proceedings in Advanced Robotics, Springer, 2017), vol. 2, pp. 5–20.
37. Z. Zhang, J. Zhao, H. Chen, D. Chen, A survey of bioinspired jumping robot: Takeoff, air posture adjustment, and landing buffer. *Appl. Bionics Biomech.* **2017**, 4780160 (2017).
38. Y. H. Tan, R. Siddall, M. Kovac, Efficient aerial-aquatic locomotion with a single propulsion system. *IEEE Robot. Autom. Lett.* **2**, 1304–1311 (2017).

Acknowledgments: R.S. is currently at the Max Planck Institute for Intelligent Systems, Stuttgart, Germany. **Funding:** The research is funded by the EPSRC [grants EP/N009061/1, EP/R026173/1, and EP/R009953/1 and Center for Doctoral Training in Fluid Dynamics across Scales (award no. EP/L016230/1)], NERC grant NE/R012229/1, and the EU H2020 AeRoTwin project (grant ID 810321). M.K. is supported by the Royal Society Wolfson Fellowship under grant agreement RSFR1180003. The Multi-Terrain Aerial Robotics Arena is supported through a philanthropic gift by B. Vasudevan. **Author contributions:** R.Z. lead the project, driving on the system development, analytical work, experiments, and writing. A.O.A. focused on the robot interaction with air and water, from CFD to design and flight experiments. A.F. brought significant advances in stability calculations and was deeply involved in fabrication and testing as well as results analysis. R.S. technically supported the whole research through his experience in aerial aquatic robotics. M.N., R.V.B., and G.K. contributed to the paper through their work on electronic design, chamber development, and theory. S.F.A.'s expertise in modeling helped to provide insights into the data and was also involved in the writing. M.K. supervised the research and provided feedback and guidance on both the scientific work and the manuscript. **Competing interests:** The authors declare that they have no competing interests. **Data and materials availability:** The data required to perform the experiments, construct a similar thruster, and verify the integrity of the reported results can be found in the Supplementary Materials.

Submitted 3 May 2019
Accepted 7 August 2019
Published 11 September 2019
10.1126/scirobotics.aax7330

Citation: R. Zufferey, A. O. Ancel, A. Farinha, R. Siddall, S. F. Armanini, M. Nasr, R. V. Brahmal, G. Kennedy, M. Kovac, Consecutive aquatic jump-gliding with water-reactive fuel. *Sci. Robot.* **4**, eaax7330 (2019).

Science Robotics

Consecutive aquatic jump-gliding with water-reactive fuel

R. Zufferey, A. Ortega Ancel, A. Farinha, R. Siddall, S. F. Armanini, M. Nasr, R. V. Brahmal, G. Kennedy and M. Kovac

Sci. Robotics **4**, eaax7330.
DOI: 10.1126/scirobotics.aax7330